Supplementary material for: BOSSE v1.0: the Biodiversity Observing System Simulation Experiment

Javier Pacheco-Labrador[1,2], Ulisse Gomarasca[2], Daniel E. Pabon-Moreno[2], Wantong Li[3], Mirco Migliavacca[4], Martin Jung[2], and Gregory Duveiller[2]

[1]Environmental Remote Sensing and Spectroscopy Laboratory (SpecLab), Spanish National Research Council (CSIC), Madrid, 28037, Spain
[2]Max Planck Institute for Biogeochemistry, Jena, D-07745, Germany
[3]Department of Environmental Science Policy and Management, UC Berkeley, Berkeley, CA, USA
[4]European Commission, Joint Research Center, Ispra, Italy

Correspondence to: Javier Pacheco-Labrador (javier.pacheco@csic.es)

The following supplementary material includes additional descriptions, tables, and figures of the BOSSE model. Supplementary (S) 1 describes the plant functional types (PFT) and how their relative abundance was calculated per climatic zone. S2 describes the meteorological variables that BOSSE uses to run. S3 reports how different spectral libraries and trait databases were processed to characterize their covariance and randomly generate draws of traits. S4 describes how the SCOPE simulations used to train the BOSSE emulators were configured and run. S5 describes the model predicting soil resistance for evaporation from the pore space. S6 reports the training of the different BOSSE emulators. S8 describes the phenological model. S8 describes the semi-empirical respiration model. S9 reports how the spatial resolution of maps and images is degraded. S10 reproduces Fig. 5 in the manuscript with “clustered” and “even” spatial patterns. S11 reproduces Fig. 6 in the manuscript with “clustered” and “even” spatial patterns. S12 shows the meteorological data used to simulate the ecosystem functions in Fig. 7 in the manuscript.

S1 Plant functional types and climatic zones

BOSSE determines the plant functional types (PFT) that could potentially exist in a simulated Scene as a function of the climatic zone where a site is located. PFT frequency per climatic zone was extracted by convolving the European Space Agency’s Land Cover Climate Change Initiative (ESA LC-CCI) Global Plant Functional Types Dataset (v.2.08) from Harper et al. (2023) with the Köppen Climate Classification System maps from Rubel et al. (2017). To do so, we averaged the annual pixel abundance of each PFT between 2000 and 2022 and combined some of the map PFTs (Table S1.1). Since the ESA LC-CCI product does not discriminate between C3 and C4 metabolic pathways, we used the estimates of C3/C4 grass leaf area fraction generated in the NACP MsTMIP simulations (Global 0.5-degree Model Outputs in Standard Format, Version 2.0, from Huntzinger et al. (2021)) to separate the Grasses PFTs. We considered four of the five main climatic zones in the Köppen classification (Tropical, Dry, Temperate, and Continental). The resulting PFT frequencies per climatic zone are presented in Table S1.1.

Table S1.1. BOSSE plant functional types and abundances per climatic zones

BOSSE PFT	ESA LC-CCI PFT	Frequency Tropical (%)	Frequency Dry (%)	Frequency Temperate (%)	Frequency Continental (%)
Deciduous Needle Forest (DNF)	TREES-ND	0.00	0.00	0.00	7.86
Evergreen Needle Forest (ENF)	TREES-NE	0.00	0.00	10.48	19.37
Deciduous Broadleaf Forest (DBF)	TREES-BD	7.36	1.45	9.67	8.09
Evergreen Broadleaf Forest (EBF)	TREES-BE	43.97	0.00	8.46	0.00
Shrubland (SHB)	SHRUBS-ND + SHRUBS-BD + SHRUBS-NE + SHRUBS-BE	4.21	6.49	2.65	5.90
C3 Grasses (GRAC3)	GRASS-MAN + GRASS-NAT	0.00	62.54	59.07	58.79
C4 Grasses (GRAC4)	GRASS-MAN + GRASS-NAT	44.46	29.52	9.67	0.00

S2 Meteorological data

BOSSE can be run at different locations where meteorological data has been evenly selected and prepared (Table S3.1) within the climatic zones. For each climatic zone, we selected 15 random locations within each climatic zone, (60 sites total). We gathered these sites' ERA5-Land hourly meteorological time series between 2020 and 2022. Accumulated radiation and precipitation variables were recomputed at hourly intervals, and these were used to produce the inputs of the model SCOPE (Van Der Tol et al., 2009) as in Li et al. (2023). These data were used for two purposes. The main one was to run BOSSE simulations. The second purpose was to fit a Gaussian Mixture Model (GMM) able to predict coherent meteorological conditions that could be used as inputs of the SCOPE model (Van Der Tol et al., 2009) look-up table simulations (Supplementary S6) used to train the emulators and (Supplementary S8). To do so, we used two ERA5-Land datasets, data from 1000 sites located in draught-prone regions downloaded for SCOPE simulations used by Li et al. (2023) and the time series downloaded at the BOSSE climatic regions. We selected 10^5 samples from these datasets to fit the GMM using the expectation-maximization (EM) algorithm (Dempster et al., 1977).

Table S2.1 BOSSE meteorological variables

Variable	ERA Variable name	Units	Description
Time	time	-	
Year	Yr	y	
DoY	DoY	d	Day of the year
Hour	Hour	h	
Latitude	latitude	º	
Longitude	longitude	º	
Air temperature	Ta	ºC	ERA5-Land 2 metre temperature (t2m)
Air pressure	p	hPa	ERA5-Land Surface pressure (sp)
Accumulated incoming shortwave irradiance	ssrd	J m^{-2}	ERA5-Land Surface solar radiation downwards (ssrd)
Accumulated incoming shortwave irradiance	strd	J m^{-2}	ERA5-Land Surface thermal radiation downwards (ssrd)
Total precipitation	tp	m	ERA5-Land Total precipitation (tp)
Relative humidity	rH	%	
Incoming shortwave irradiance	Rin	W m^{-2}	Instantaneous (desaccumulation of ssrd)
Incoming longwave irradiance	Rli	W m^{-2}	Instantaneous (desaccumulation of strd)
Sun zenith angle	tts	º	Computed with the Python package "pysolar"
Sun azimuth angle	saa	º	Computed with the Python package "pysolar"
Vapor pressure	ea	hPa	Calculated from Ta and rH
Wind speed	u	m s^{-1}	Vector addition of ERA5-Land 10 metre U wind component (u10) and 10 metre V wind component (v10)
Volumetric soil moisture content	SMC	%	Averaged ERA5-Land Volumetric soil water layer 1 (swvl1), Volumetric soil water layer 2 (swvl2), Volumetric soil water layer 3 (swvl3), and Volumetric soil water layer 4 (swvl4).
Relative soil moisture	wr	-	Volumetric soil moisture content to field capacity
Vapor pressure deficit	VPD	hPa	Calculated from Ta and ea
Potential evapotranspiration	PET	mm d^{-1}	Computing using the Penman-Monteith model in the Python package "pyet"
Day time	DayTime	-	Boolean, whether Rin > W m^{-2}

S3 Plant traits and covariance

To randomly sample realistic sets of plant traits, we generated a dataset of foliar traits and radiative transfer parameters by combining spectral libraries and samples from the TRY database (Kattge et al., 2020). Then, we adjusted a GMM over this dataset as before. First, we gathered the spectral libraries LOPEX (Hosgood et al., 1994) and ANGERS (Feret et al., 2008), which offered 606 sets of leaf directional-hemispherical reflectance and transmittance factors and RTM parameters as in Pacheco-Labrador et al. (2022). However, some missing parameters were estimated this time instead of assumed to equal 0. We estimated leaf anthocyanin content (C_{ant}) using the linear equation adjusted for the modified Anthocyanin Reflectance Index (mARI) as in Féret et al. (2017). We gap-filled any other missing parameter (mostly senescent pigments (C_{s})) by inverting the leaf radiative transfer model PROSPECT-D (Féret et al., 2017). However, since the PROSPECT model (Jacquemoud and Baret, 1990) has evolved, changing some of the initial assumptions regarding surface rugosity and illumination angles (Feret et al., 2008), we first re-calculated the leaf structural parameter (N) inverting the model against the three wavelengths with minimum absorptance or maximum transmittance or reflectance as described in Féret et al. (2017), and then constrained the missing parameters. If the fit RMSE was larger than 0.0025, we considered that C_{s} could be large enough to affect the retrieval of N, and attempted to constrain simultaneously C_{s} and N against the three selected wavelengths. If RMSE was still larger than the threshold, we assumed pigment measurements could be uncertain and, therefore, attempted to constrain all pigments and N simultaneously against the leaf optical properties available between 400 and 1050 nm. We kept 591 samples with root mean squared error (RSME) lower than 0.0025; the removed samples corresponded to quite senesced leaves, which likely could not be fit due to the fact senescent pigments darken over time (Proctor et al., 2017; Pacheco-Labrador et al., 2021).

We also incorporated additional spectral libraries featuring 203 sets of foliar visible and near-infrared reflectance factors and measurements of chlorophyll (C_{ab}), carotenoids (C_{ar}), and C_{ant} content (Gitelson et al., 2017; Solovchenko et al., 2017). To gap-fill dry matter (C_{dm}) and (C_{w}) content, with little influence in the available spectral range, we used the data available from the previous gap-filled databases to train variational heteroscedastic Gaussian process (VHGP) models (Lázaro-Gredilla et al., 2014) to predict C_{w} as a function of N, and C_{ab} (test squared Pearson correlation coefficient $r^2 = 0.69$, relative root mean squared error RRMSE = 32.9 %) and C_{dm} as a function of N, C_{ab}, C_{ar}, and C_{ant} (test $r^2 = 0.69$, RRMSE = 32.3 %, respectively). These models were used to predict these plant traits during the inversion of PROSPECT-D and to determine the final values after optimization. We used the same methodology described before, but using only reflectance factors with sufficient quality between 437 and 900 nm. In this case, all the samples featured RMSE < 0.0025. In total, the spectral libraries offered 794 samples.

We extracted foliar pigments, dry matter (or specific leaf area), and water available per mass, area, or nitrogen content data from the TRY database (TraitID ∈ [413, 164, 418, 491, 809, 810, 731, 3120, 3115, 3116, 3117, 185, 186, 487, 50, 14], accessed in October 2022), which led to a dataset of 370096 samples of foliar radiative model parameters where N and C_{s} were missing in all the cases. We kept 15935 samples presenting at least C_{ab} or C_{ar} and C_{dm} or C_{w} values. C_{ab} and C_{dm} were available for all these samples. Then, data were gap-filled with VHGP models (Table S3.1) trained from the values available within the 16703 samples of the joint datasets (spectral libraries and TRY).

Table S3.1. VHGP models trained on the joint spectral and TRY databases. * means that gap-filled data were used to train the model.

Predicted variable	Predictors	Train statistics	Test statistics
C_{ar}	C_{ab}, C_{dm}	$r^2 = 0.85$ RRMSE = 23.7 %	$r^2 = 0.76$ RRMSE = 30.2 %
C_w	C_{ab}, C_{dm}	$r^2 = 0.59$ RRMSE = 47.2 %	$r^2 = 0.59$ RRMSE = 48.7 %
N	C_{ab}, C_{ar}^*, C_w^*, C_{dm}	$r^2 = 0.77$ RRMSE = 8.7 %	$r^2 = 0.53$ RRMSE = 12.3 %
C_s	N^*, C_{ab}, C_w^*, C_{dm}	$r^2 = 0.47$ RRMSE = 97.9 %	$r^2 = 0.32$ RRMSE = 99.7 %
C_{ant}	N^*, C_{ab}, C_{ar}^*, C_s^*, C_w^*	$r^2 = 0.26$ RRMSE = 236.8 %	$r^2 = 0.29$ RRMSE = 242.0 %

Additional relevant parameters of the model, such as the maximum carboxylation rate (V_{cmax}) and the Ball-Berry stomatal sensitivity (m_{BB}), were generated from different sources. Miner et al. (2016) provided plant functional type-dependent ranges of variability from where m_{BB} could be randomly sampled. Luo et al. (2019) provided linear model coefficients to predict V_{cmax} from C_{ab} for C3 plants; for C4 grasses, we scaled multiplying by 0.28, a C4/C3 ratio reported by Niu et al. (2006). Moreover, for the leaf area index (LAI), the maximum values were set by Asner et al. (2003) as a function of the PFT and the climatic zone. We used the maximum values corrected by using a two inter-quartile range analysis (Table 2 in Asner et al. (2003)).

S4 SCOPE simulations

We used the model SCOPE v1.74 (Van Der Tol et al., 2009) to generate look-up tables (LUT) of 10^4 samples of vegetation and soil parameters, meteorological conditions, and the corresponding spectral signals with two different configurations using a Gaussian Mixture Model (GMM, Supplementary S3. Plant traits and covariance) and a Latin Hypercube Sampling (LHS) approach. In all cases, LHS was used to create the structural parameters such as LAI, LIDF_a, LIDF_b, h_c, and l_w. We also included an empirical parameter determining the sensitivity of soil resistance for evaporation from the pore space (r_{ss}) to relative soil moisture content (the ratio between soil moisture content (SM_p) and field capacity (θ_{fc}), that determined r_{ss} as a function of the former ones (Supplementary S5. Soil resistance for evaporation from the pore space model). Furthermore, we included the stress factor introduced in SCOPE by Bayat et al. (2019), which reduces the maximum carboxylation rate as a function of soil moisture content. This variable allows simulations to include a direct link between plant physiological regulation with fluorescence radiance and surface temperature. Since this factor varies between 0 and 1, BOSSE simulations directly prescribed the stress factor with the value of the GSI response function to water availability. Leaf and soil thermal emissivities were prescribed as a function of their reflectance factor at 2400 nm to make this variable controlling energy balance and surface temperature more dynamic and linked to vegetation properties. Separated models were calibrated with the samples of soil (R^2 = 0.76, RMSE = 0.008) and photosynthetic vegetation (R^2 = 0.46, RMSE = 0.018) available in the

ECOSTRESS spectral library version 1.0 (Meerdink et al., 2019). The meteorological inputs were always drawn from the GMM generated from the ERA-5 Land datasets (Supplementary S2. Meteorological data). We included a LUT of 4000 samples simulating bare soil to improve the performance of the models at low LAI values.

SCOPE predicted hyperspectral reflectance factors (R) and sun-induced chlorophyll radiances (F). In addition, we produced an estimate of land surface temperature (LST) by applying the temperature-emissivity separation (TES) algorithm (Hanuš et al., 2016) to the bottom of the atmosphere thermal radiances provided by SCOPE. Both LUTs were produced to train the emulators. In addition, we generated smaller LUTs (5000 samples) using the same approaches for testing the emulators and 2000 samples of bare-soil LUTs that were added to the training and test datasets. The latest improved the emulators' performance when *LAI* was low.

We then trained emulators (2-layer neural networks) to predict these variables individually (R, F, LST) and to estimate vegetation foliar and structural variables (OT) from the hyperspectral R and from these convolved to the spectral configuration of different imagers: EnMAP, DESIS, and Sentinel-2 MSI (Supplementary S6. SCOPE emulators).

S5 Soil resistance for evaporation from the pore space model

We developed a semi-empirical model predicting soil resistance for evaporation from the pore space (r_{ss}) as a function of relative soil water content (SM_{rel}, the ratio of soil moisture content (SM_p), and field capacity (θ_{fc})) and a sensitivity parameter ($r_{ss,factor}$). Unlike former models used for this purpose in SCOPE (e.g., Pacheco-Labrador et al. (2019)), this model includes a parameter controlling the sensitivity of the resistance to water availability, which allows for multiple soil responses. The model is a 2D interpolator that uses simulated curves at fixed $r_{ss,factor}$ values (Fig. S6.1)

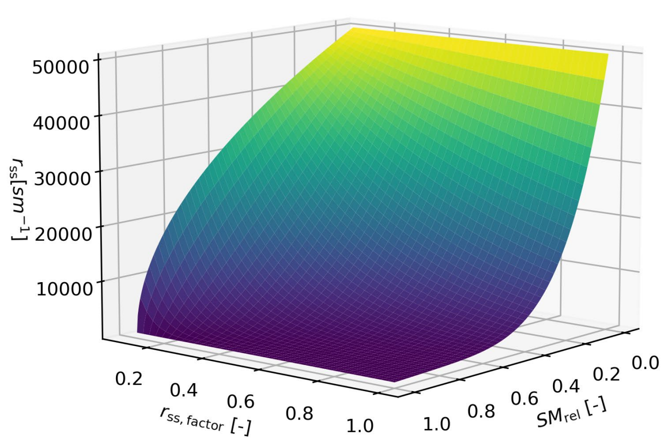

Figure S6.1: 2D interpolator predicting soil resistance for evaporation from the pore space as a function of relative soil water content and a sensitivity parameter.

S6 SCOPE emulators

Three emulators (2-layer neural networks) predicting hyperspectral reflectance factors (R), hyperspectral sun-induced chlorophyll radiances (F), and land surface temperature (LST) were trained from the SCOPE look-up tables (LUT) (Supplementary S4. SCOPE simulations). From the $22 \cdot 10^4$ samples available for training each emulator, 20 % was left apart for validation during the optimization of the model hyperparameters (number of neurons per layer). Learning was facilitated by setting 0 for all the vegetation parameters whenever LAI was 0. Sun zenith angle (θ_{sun}) was also set to 0 whenever θ_{sun} = for the R and F emulators since the SCOPE soil reflectance model (BSM) lacks directionality and emits no fluorescence. The meteorological variables, predictors of F and LST, were set to 0 only for the first case since these, together with θ_{sun}, also play a role in LST.

Before training, random white noise (1%) was added to the spectral variables, and standardization and principal components analyses were applied to reduce dimensionality, as in Pacheco-Labrador et al. (2022). In addition, we trained 2-layer neural networks predicting vegetation foliar and structural variables from the hyperspectral R (simulated at 1 nm step) and from these reflectance factors convolved to the spectral configuration of different imagers (EnMAP, DESIS, and Sentinel-2). Standardization and PCA were also applied to the predicted variables in this case.

After that, the effect of the emulator on the estimation of functional diversity metrics was assessed using the test dataset to randomly simulate combinations of species and compute Rao's quadratic entropy index (Q_{Rao}) and the fractions of alpha and beta diversity ($f_{\alpha,\beta}$) using a variance partitioning approach implemented in the Python package "pyGNDiv" (https://github.com/JavierPachecoLabrador/pyGNDiv-master) (Pacheco-Labrador et al., 2023). We compared the metrics computed from the test look-up table variables and the corresponding emulator predictions for the evaluation.

Table S6.1 summarizes the training and test performance of the different emulators. The uncertainties of the forward emulators (predicting R, F, and LST) are low and scale according to the uncertainties expected for the corresponding RS imagery, being the largest for F and the lowest for R. In all cases, the impact of the emulator on the calculation of functional diversity metrics is low (RRMSE ≤ 1.6%). Uncertainties are larger for the models retrieving optical traits from the R convolved to different RS missions. These are particularly large for DESIS since they do not cover the shortwave infrared region, and the plant traits considered include foliar water and dry matter contents, which affect that region most strongly. Despite the larger prediction uncertainties, the impact on the computation of FDM is similarly low (RRMSE ≤ 3.6%). Table S6.2 summarizes the training and test performance of the emulator that predicts most of the ecosystem functions. For all the variables, train $R^2 \geq 0.98$, except for sensible heat flux (H, $R^2 = 0.97$), and test $R^2 \geq 0.95$, except for H ($R^2 = 0.92$). The performance of the model is within what could be expected from eddy covariance measurements.

Table S6.1. Performance of the different remote sensing SCOPE emulators

Emulator	Predicted variable	Predictors	Train RRMSE (%)	Test RRMSE (%)	Test Q_{Rao} RRMSE (%)	Test $f_{\alpha,\beta}$ RRMSE (%)
Reflectance factors	R	RTM plant and soil variables, and sun-view geometry	1.83	2.19	0.05	0.01
Fluorescence radiance	F	RTM plant, soil, meteorological variables, and sun-view geometry	5.77	11.37	1.60	0.20
Land surface temperature	LST	RTM plant, soil, meteorological variables, and sun-view geometry	2.81	3.09	1.05	0.37
Optical trait retrieval (Hyperspectral)	OT_{Hy}	R and sun-view geometry	20.32	23.40	1.66	0.44
Optical trait retrieval (EnMAP)	OT_{EnMAP}	R and sun-view geometry	25.57	27.79	2.18	0.54
Optical trait retrieval (DESIS)	OT_{DESIS}	R and sun-view geometry	29.68	31.92	2.79	0.65
Optical trait retrieval (Sentinel-2)	OT_{S2}	R and sun-view geometry	33.57	35.42	3.59	0.73

Table S6.2 Performance of the different ecosystem functions SCOPE emulator

Variable	Predicted variable	Units	Predictors	Train RMSE	Test RMSE	Train RRMSE (%)	Test RRMSE (%)
Gross primary production	GPP	μmolC m^{-2} s^{-1}	RTM plant, soil, meteorological variables, and sun-view geometry	1.38	2.05	18.38	29.03
Total latent heat flux	λ	W m^{-2}		21.55	35.02	17.91	31.37
Transpiration	λ_{canopy}	W m^{-2}		21.54	34.42	19.26	33.56
Sensible heat flux	H	W m^{-2}		21.78	33.20	25.49	41.01
Net radiation	R_n	W m^{-2}		11.40	12.78	5.22	6.20
Soil heat flux	G_{tot}	W m^{-2}		2.34	2.64	18.05	19.46
Light-use efficiency	LUE	μmolC μmol^{-1}				10.05	16.75
Green light-use efficiency	LUE_{green}	μmolC μmol^{-1}				8.41	19.78

S7 The Growing Season Index phenological model

The Growing Season Index (GSI) phenological model (Forkel et al., 2014) defines vegetation phenology as a function of its response to light (i.e., incoming shortwave radiation (R_{in})), water availability (w_{av}), to cold and heat determined by air temperature (T_{a}). The phenological response to each of these responses takes the shape (Eq. S7.1):

$$f_{x,\mathrm{PFT}}^{t} = f_{x,\mathrm{PFT}}^{t-1} + \left(\frac{1}{1+e^{\left(\alpha \cdot s_{x,\mathrm{PFT}} \cdot (x - b_{x,\mathrm{PFT}})\right)}} - f_{x,\mathrm{PFT}}^{t-1}\right) \cdot \tau_{x,\mathrm{PFT}}\ , \quad \text{(S7.1)}$$

where f stands for the vegetation response, t for the current timestep and t-1 for the former one, x for the environmental driver (R_{in}, w_{av}, or T_{a}), $s_{x,\mathrm{PFT}}$ for the slope, $b_{x,\mathrm{PFT}}$ for the base or inflection point, and $\tau_{x,\mathrm{PFT}}$ is the sensitivity respect to the former conditions, where under scripts x and PFT indicate that their values are driver and PFT-dependent. The coefficient a equals -1 for all the responses except for the one to heat, which presents a negative response to the driver. The absolute value of the second addend in Eq. S8.1 was truncated using PFT-dependent values to prevent unrealistic changes in the physiological state of vegetation (Table S7.1).

Table S7.1. GSI rate of change limits per plant functional type in [day-1].

DNF	ENF	DBF	EBF	SHB	GRAC3	GRAC4
0.015	0.008	0.015	0.008	0.015	0.025	0.025

These functions scale between 0 and 1, and the model determines the final phenological state of vegetation, which is the product of the four responses (Eq. S7.2).

$$GSI_{\mathrm{PFT}} = f_{\mathrm{light,PFT}} \cdot f_{\mathrm{water,PFT}} \cdot f_{\mathrm{cold,PFT}} \cdot f_{\mathrm{heat,PFT}}, \quad \text{(S7.2)}$$

Forkel et al. (2014) constrained the PFT-dependent parameters of the model ($s_{x,\mathrm{PFT}}$, $b_{x,\mathrm{PFT}}$, $\tau_{x,\mathrm{PFT}}$) against time series of the fraction of absorbed photosynthetically active radiation (f_{aPAR}), considering this variable integrative of the phenological response of function vegetation to the environment since it determines the amount of radiation vegetation aims to absorb as a function of its capability to use it for photosynthesis. Whereas f_{aPAR} cannot summarize all the vegetation functions, we considered this variable enough to represent plant traits phenology in BOSSE. Parameter values are defined per species and plant trait.

S8 Ecosystem respiration model

Since SCOPE does not predict ecosystem respiration (R_{eco}) we implemented the semi-empirical model of Migliavacca et al. (2011). The model predicts respiration at a daily scale as a function of different physical and empirical factors (Eq. S8.1)

$$R_{\mathrm{eco}} = (R_{\mathrm{LAI=0}} + a_{\mathrm{LAI}} \cdot \mathrm{LAI}_{\mathrm{max}} + k_2 \cdot \mathrm{GPP}) \cdot e^{E_0\left(\frac{1}{T_{\mathrm{ref}}-T_0} - \frac{1}{T_{\mathrm{a}}-T_0}\right)} \cdot \left(\frac{\alpha \cdot K + P(1-\alpha)}{K + P(1-\alpha)}\right) \quad \text{(s8.1)}$$

where R_{eco} depends on the leaf area index (LAI) and gross primary production (GPP), air temperature (T_a), and precipitation (P). LAI and GPP response is given by a basal respiration level given by R_{eco} when LAI = 0 ($R_{LAI=0}$, the sensitivity to LAI (a_{LAI}), and a GPP-related sensitivity (k_2). T_a dependency is expressed by an exponential function of the product between the ecosystem respiration sensitivity to temperature (or activation energy parameter E_0) and the difference between the inverse differences of a reference temperature (T_{ref} = 288.15 K) and T_a with another fixed temperature (T_0 = 227.13 K). Finally, precipitation effects are defined with a hyperbolic function controlled by the half-saturation constant (k) and the R_{eco} response to null precipitation (α). Since the model predicts daily Reco, for each hourly timestamp, the T_a averaged the 24 h around the timestamp, the accumulated GPP in the 24 h surrounding the timestamp, and the 30 days averaged precipitation are used to compute the respiration rate. Then, the model day-based output in [gC m^{-2} day^{-1}] are converted to instantaneous rates [μmolC m^{-2} s^{-1}].

We use the PFT-specific parameter values from Table 5 in Migliavacca et al. (2011) and the standard errors estimated to draw each species' parameters randomly. Intra-specific variability is generated by considering it is between 20 % and 40 % of the interspecific variability (Albert et al., 2010). The specific value is determined randomly for each species' individual. For all the parameters except $R_{LAI=0}$, negative values are avoided by taking the absolute value, moreover, α is truncated between [0.05, 0.95] to prevent too extreme responses. These values are summarized in Table S8.1. LAI_{max} is directly assigned from the upper bound of LAI assigned to each individual.

Table S8.1. Mean and standard deviation used to assign the ecosystem respiration model values using a Normal distribution.

Param.	DNF	ENF	DBF	EBF	SHB	GRAC3	GRAC4
$R_{\mathrm{LAI=0}}$	μ=1.02 σ=0.42	μ=1.02 σ=0.42	μ=1.20 σ=0.50	μ=-047 σ=0.50	μ=0.42 σ=0.39	μ=0.42 σ=0.71	μ=0.42 σ=0.71
a_{LAI}	μ=0.42 σ=0.08	μ=0.42 σ=0.08	μ=0.34 σ=0.10	μ=0.82 σ=0.13	μ=0.57 σ=0.17	μ=1.14 σ=0.33	μ=1.14 σ=0.33
k_2	μ=0.478 σ=0.013	μ=0.478 σ=0.013	μ=0.247 σ=0.009	μ=0. 602 σ=0. 044	μ=0.354 σ=0.021	μ=0.578 σ=0.062	μ=0.578 σ=0.062
E_0	μ=124.833 σ=4.656	μ=124.833 σ=4.656	μ=87.655 σ=4.405	μ=52.753 σ=4.351	μ=156.746 σ=8.222	μ=101.181 σ=6.362	μ=101.181 σ=6.362
α	μ=0.604 σ=0.065	μ=0.604 σ=0.065	μ=0.796 σ=0.031	μ=0.593 σ=0.032	μ=0.850 σ=0.070	μ=0.670 σ=0.052	μ=0.670 σ=0.052
K	μ=0.222 σ=0.070	μ=0.222 σ=0.070	μ=0.184 σ=0.064	μ=2.019 σ=1.052	μ=0.097 σ=1.304	μ=0.765 σ=1.589	μ=0.765 σ=1.589

S9 Remote sensing spatial resolution degradation

BOSSE remote sensing imagery spatial resolution can be downgraded using a Gaussian point spread function (PSF) model to more accurately mimic the spatial artifacts that can occur due to the gridding step that separates remote sensing observations from the resulting gridded imagery (Wang et al., 2020; Duveiller et al., 2011). BOSSE spatial resolution (r_{spat}) is defined as the ratio of the simulation (plant) to the pixel size; therefore, a 100 % resolution implies that each pixel contains unmixed information of a unique individual or set of identical individuals. This is accounted for by the standard deviation (σ_{PSF}) and sampling interval of the PSF. The PSF is truncated at $4\sigma_{\mathrm{PSF}}$ to ensure no mixture at r_{spat} = 100 %, and σ_{PSF} is defined as (1 / 4) / (100 / r_{spat}). The sampling points ([x_0, y_0], the center of the PSF at each remote sensing pixel, are evenly distributed between 100 / r_{spat} and the size of the output remote sensing image ($n_{\mathrm{pix,image}} = r_{\mathrm{spat}} \cdot n_{\mathrm{pix,\ Scene}}$) with a step equal to 100 / r_{spat}. This way, for r_{spat} = 100 %, the center of each image pixel matches the center of the simulated scene pixel.

$$PSF_{x,y} = \mathcal{N}\left([x_o, y_o], \begin{bmatrix} \sigma_{\mathrm{PSF}} & 0 \\ 0 & \sigma_{\mathrm{PSF}} \end{bmatrix}\right), \qquad \text{(S10.1)}$$

S10 BOSSE maps

Example of the simulation of Scene maps with “clustered” (Fig. S10.1) and “even” (Fig. S10.2) spatial patterns. The figures are comparable to Fig. 4 in the manuscript.

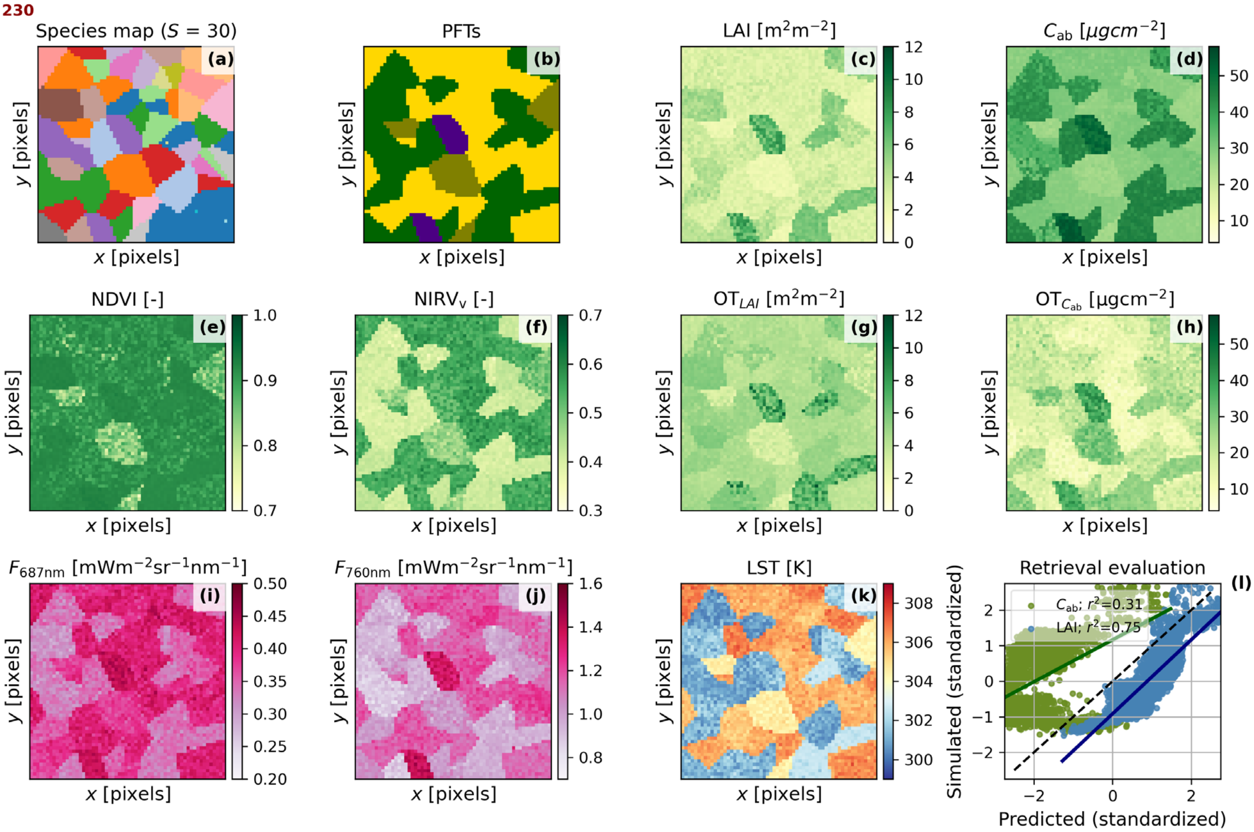

Figure 10.1: Simulated scene located in Continental climate and an “clustered” spatial pattern at midday of the day 230 of the time series presented in Fig. 2b,h. The coordinates are shown in pixels. Maps of species, indicating taxonomical Richness (*S*) (a), species' plant functional types (b), leaf area index (c), foliar chlorophyll content (d), normalized difference vegetation index (e), near-infrared reflectance of vegetation index (f), estimated leaf area index (g), estimated foliar chlorophyll content (h), fluorescence radiance at 687 nm (i), fluorescence radiance at 760 nm (j), land surface temperature (k), and the predicted vs. simulated leaf area index and foliar chlorophyll content (l), standardized for comparison and evaluated with the Pearson correlation coefficient (r^2).

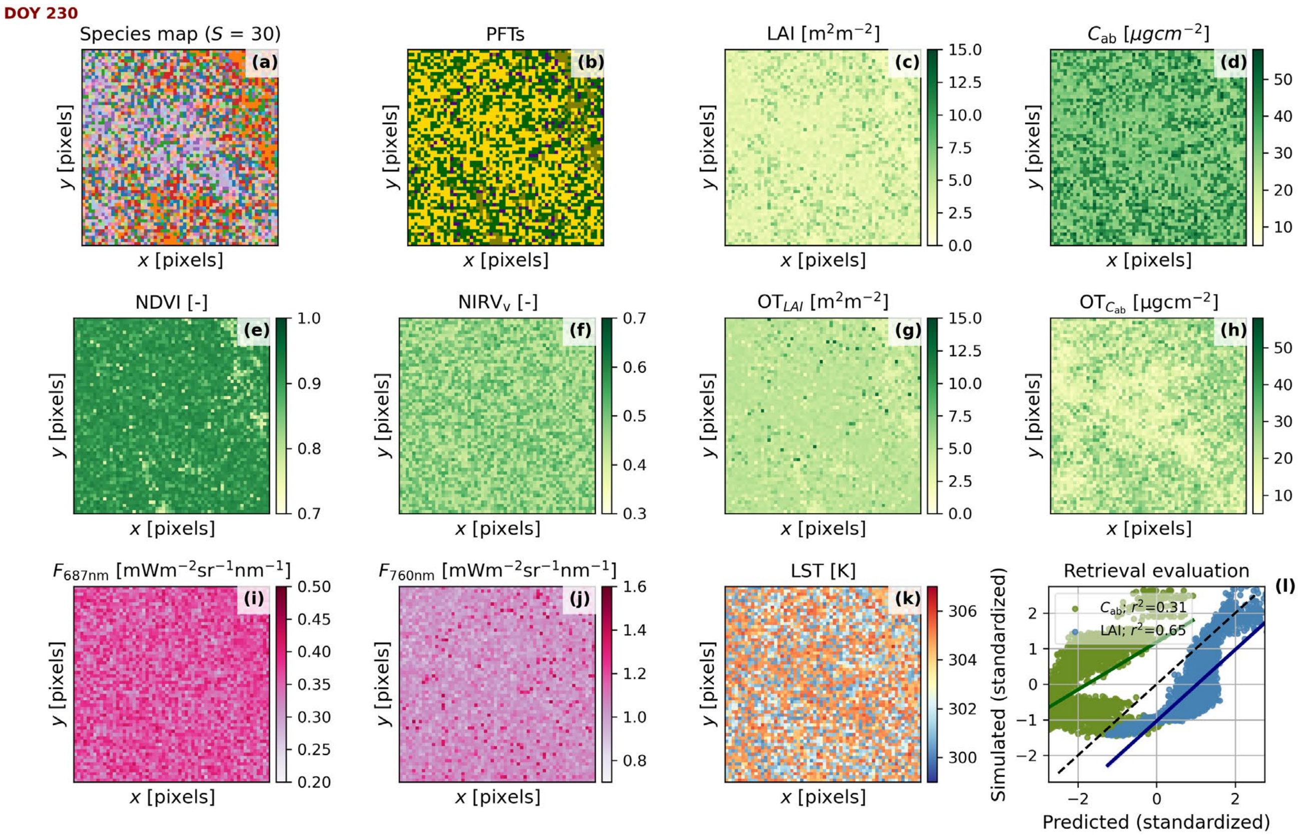

Figure 10.2: Simulated scene located in Continental climate and an "even" spatial pattern at midday of the day 230 of the time series presented in Fig. 2b,h. The coordinates are shown in pixels. Maps of species, indicating taxonomical Richness (*S*) (a), species' plant functional types (b), leaf area index (c), foliar chlorophyll content (d), normalized difference vegetation index (e), near-infrared reflectance of vegetation index (f), estimated leaf area index (g), estimated foliar chlorophyll content (h), fluorescence radiance at 687 nm (i), fluorescence radiance at 760 nm (j), land surface temperature (k), and the predicted vs. simulated leaf area index and foliar chlorophyll content (l), standardized for comparison and evaluated with the Pearson correlation coefficient (r^2).

S11 Examples of spatial resolution degradation effect on the functional diversity estimates

Example of the of spatial resolution degradation effect on the functional diversity estimates with "clustered" (Fig. S11.1) and "even" (Fig. S11.2) spatial patterns. The figures are comparable to Fig. 5 in the manuscript.

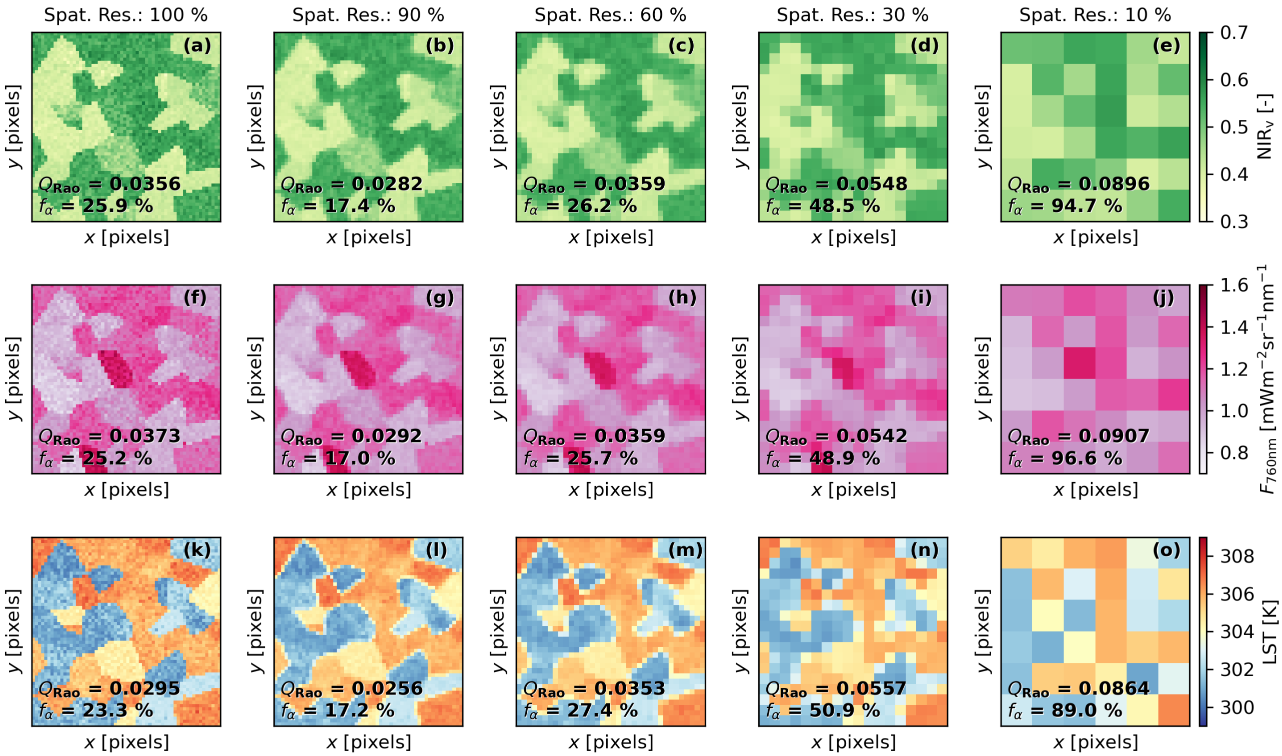

Figure 11.1: Simulated imagery of the near-infrared of vegetation index (a-e), fluorescence radiance at 760 nm (f-j), and land surface temperature (l-o) using an "clustered" spatial pattern at different spatial resolutions (100%, 90%, 60%, 30%, and 10%), defined as the plant-to-pixel size ratio. The mean value of Rao's quadratic entropy (Q_{Rao}) calculated over a 3 × 3 pixels moving window and the fraction of α-diversity (f_α), calculated from the variance-based partition approach, are presented for each map. The coordinates are shown in pixels.

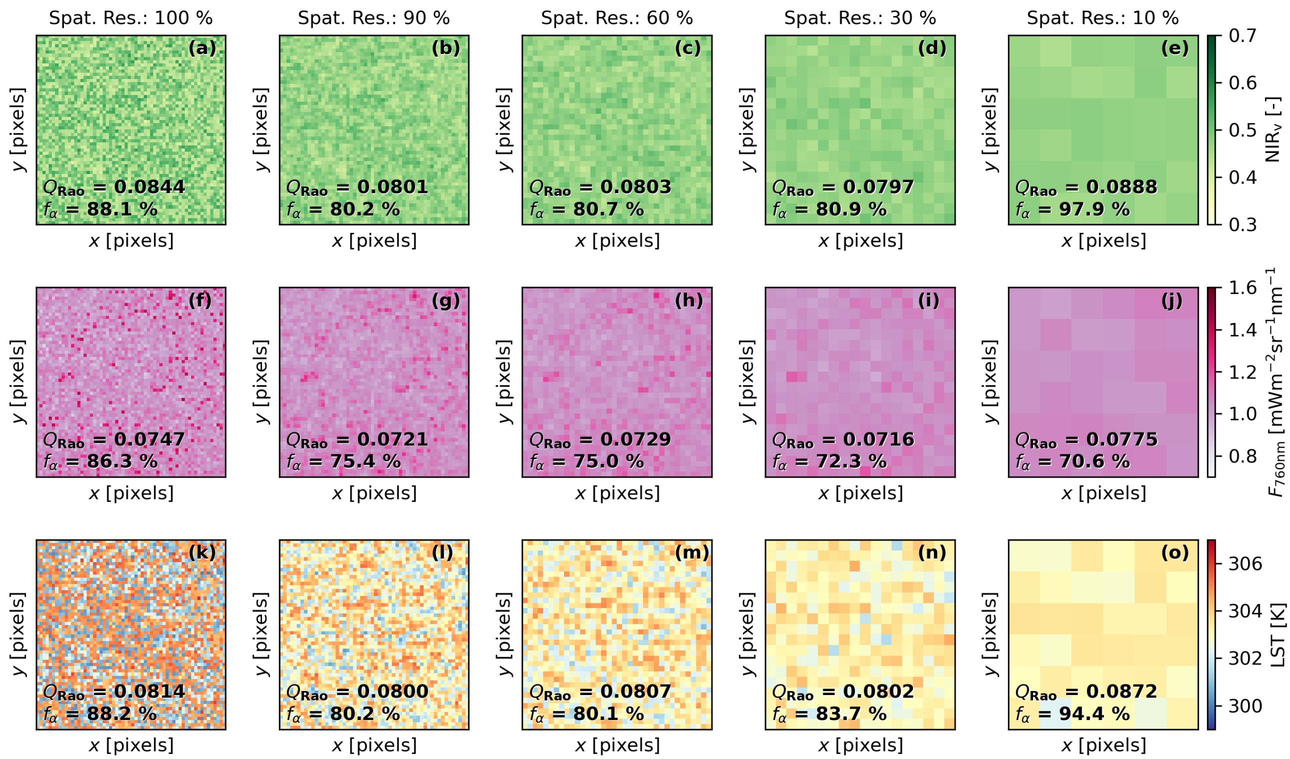

Figure 11.2. Simulated imagery of the near-infrared of vegetation index (a-e), fluorescence radiance at 760 nm (f-j), and land surface temperature (l-o) using an "even" spatial pattern at different spatial resolutions (100%, 90%, 60%, 30%, and 10%), defined as the plant-to-pixel size ratio. The mean value of Rao's quadratic entropy (Q_{Rao}) calculated over a 3 × 3 pixels moving window and the fraction of α-diversity (f_α), calculated from the variance-based partition approach, are presented for each map. The coordinates are shown in pixels.

S12 Scene meteorology

Fig. S12 presents the meteorological variables corresponding the simulations of ecosystem functions shown in Fig. 6 of the manuscript.

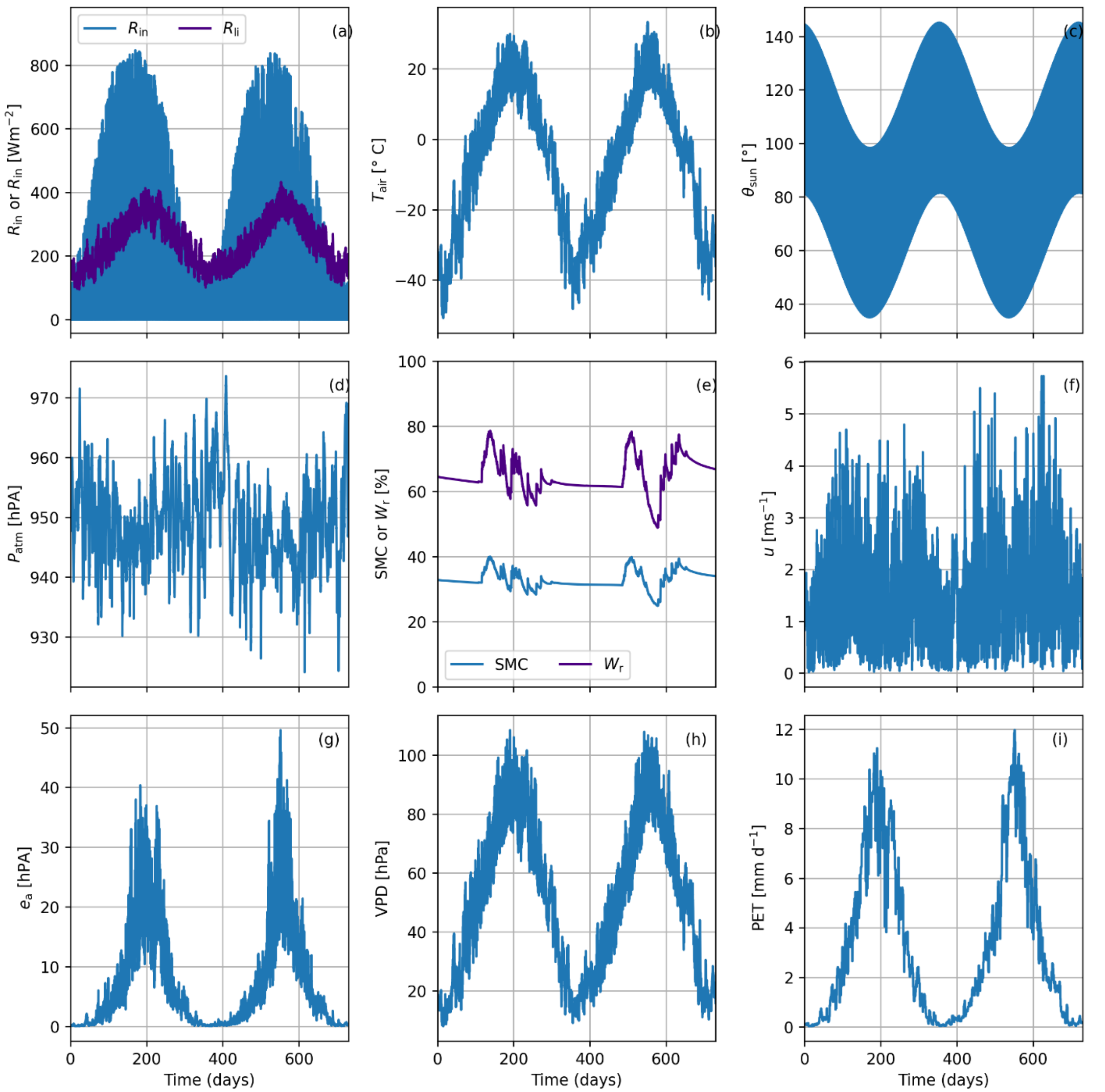

Figure S12: Meteorological data corresponding to the dataset "0" of the "Continental" short (R_{in}) and long (R_{li}) wave incoming radiation (a), air temperature (T_{air}) (b), sun zenith angle (θ_{sun}) (c), atmospheric pressure (P_{atm}) (d), soil moisture content (SMC) and water availability (W_r) (e), wind speed (u) (f), vapour pressure (e_a) (g), vapour pressure deficit (VPD) (h), and potential evapotranspiration (PET) (i).

References

Albert, C. H., Thuiller, W., Yoccoz, N. G., Douzet, R., Aubert, S., and Lavorel, S.: A multi-trait approach reveals the structure and the relative importance of intra- vs. interspecific variability in plant traits, Functional Ecology, 24, 1192-1201, https://doi.org/10.1111/j.1365-2435.2010.01727.x, 2010.

Asner, G. P., Scurlock, J. M. O., and A. Hicke, J.: Global synthesis of leaf area index observations: implications for ecological and remote sensing studies, Global Ecology and Biogeography, 12, 191-205, https://doi.org/10.1046/j.1466-822X.2003.00026.x, 2003.

Bayat, B., van der Tol, C., Yang, P., and Verhoef, W.: Extending the SCOPE model to combine optical reflectance and soil moisture observations for remote sensing of ecosystem functioning under water stress conditions, Remote Sensing of Environment, 221, 286-301, https://doi.org/10.1016/j.rse.2018.11.021, 2019.

Dempster, A. P., Laird, N. M., and Rubin, D. B.: Maximum Likelihood from Incomplete Data via the EM Algorithm, Journal of the Royal Statistical Society. Series B (Methodological), 39, 1-38, 1977.

Duveiller, G., Baret, F., and Defourny, P.: Crop specific green area index retrieval from MODIS data at regional scale by controlling pixel-target adequacy, Remote Sensing of Environment, 115, 2686-2701, https://doi.org/10.1016/j.rse.2011.05.026, 2011.

Feret, J.-B., François, C., Asner, G. P., Gitelson, A. A., Martin, R. E., Bidel, L. P. R., Ustin, S. L., le Maire, G., and Jacquemoud, S.: PROSPECT-4 and 5: Advances in the leaf optical properties model separating photosynthetic pigments, Remote Sensing of Environment, 112, 3030-3043, http://dx.doi.org/10.1016/j.rse.2008.02.012, 2008.

Féret, J. B., Gitelson, A. A., Noble, S. D., and Jacquemoud, S.: PROSPECT-D: Towards modeling leaf optical properties through a complete lifecycle, Remote Sensing of Environment, 193, 204-215, https://doi.org/10.1016/j.rse.2017.03.004, 2017.

Forkel, M., Carvalhais, N., Schaphoff, S., v. Bloh, W., Migliavacca, M., Thurner, M., and Thonicke, K.: Identifying environmental controls on vegetation greenness phenology through model–data integration, Biogeosciences, 11, 7025-7050, 10.5194/bg-11-7025-2014, 2014.

Gitelson, A., Chivkunova, O., Merzlyak, M., and Solovchenko, A.: Dataset of foliar reflectance spectra and corresponding pigment contents for Aesculus hippocastanum, Fagus Silvatica, Acer platanoides published widely [dataset], 10.13140/RG.2.2.30471.09129, 2017.

Hanuš, J., Fabiánek, T., and Fajmon, L.: POTENTIAL OF AIRBORNE IMAGING SPECTROSCOPY AT CZECHGLOBE, Int. Arch. Photogramm. Remote Sens. Spatial Inf. Sci., XLI-B1, 15-17, 10.5194/isprs-archives-XLI-B1-15-2016, 2016.

Harper, K. L., Lamarche, C., Hartley, A., Peylin, P., Ottlé, C., Bastrikov, V., San Martín, R., Bohnenstengel, S. I., Kirches, G., Boettcher, M., Shevchuk, R., Brockmann, C., and Defourny, P.: A 29-year time series of annual 300 m resolution plant-functional-type maps for climate models, Earth Syst. Sci. Data, 15, 1465-1499, 10.5194/essd-15-1465-2023, 2023.

Hosgood, B., Jacquemoud, S., Andreoli, G., Verdebout, J., Pedrini, G., and Schmuck, G.: Leaf Optical Properties EXperiment 93 (LOPEX93), 1994.

Huntzinger, D. N., Schwalm, C. R., Wei, Y., Shrestha, R., Cook, R. B., Michalak, A. M., Schafer, K. V. R., Jacobson, A. R., Arain, M. A., Ciais, P., Fisher, B. D., Kolus, H., Sikka, M., Elshorbany, Y., Hayes, D. J., Huang, M., Huang, S., Ito, A., Jain, A. K., Lei, H., Lu, C., Maignan, F., Mao, J., Parazoo, N. C., Peng, C., Peng, S., Poulter, B., Ricciuto, D. M., Tian, H., Shi, X., Wang, W., Zeng, N., Zhao, F., Zhu, Q., Yang, J., and Tao, B.: NACP MsTMIP: Global 0.5-degree Model Outputs in Standard Format, Version 2.0, 10.3334/ORNLDAAC/1599, 2021.

Jacquemoud, S. and Baret, F.: PROSPECT: A model of leaf optical properties spectra, Remote Sensing of Environment, 34, 75-91, https://doi.org/10.1016/0034-4257(90)90100-Z, 1990.

Kattge, J. and Bönisch, G. and Díaz, S. and Lavorel, S. and Prentice, I. C. and Leadley, P. and Tautenhahn, S. and Werner, G. D. A. and Aakala, T. and Abedi, M. and Acosta, A. T. R. and Adamidis, G. C. and Adamson, K. and Aiba, M. and Albert, C. H. and Alcántara, J. M. and Alcázar C, C. and Aleixo, I. and Ali, H. and Amiaud, B. and Ammer, C. and Amoroso, M. M. and Anand, M. and Anderson, C. and Anten, N. and Antos, J. and Apgaua, D. M. G. and Ashman, T.-L. and Asmara, D. H. and Asner, G. P. and Aspinwall, M. and Atkin, O. and Aubin, I. and Baastrup-Spohr, L. and Bahalkeh, K. and Bahn, M. and Baker, T. and Baker, W. J. and Bakker, J. P. and Baldocchi, D. and Baltzer, J. and Banerjee, A. and Baranger, A. and Barlow, J. and Barneche, D. R. and Baruch, Z. and Bastianelli, D. and Battles, J. and Bauerle, W. and Bauters, M. and Bazzato, E. and Beckmann, M. and Beeckman, H. and Beierkuhnlein, C. and Bekker, R. and Belfry, G. and Belluau, M. and

Beloiu, M. and Benavides, R. and Benomar, L. and Berdugo-Lattke, M. L. and Berenguer, E. and Bergamin, R. and Bergmann, J. and Bergmann Carlucci, M. and Berner, L. and Bernhardt-Römermann, M. and Bigler, C. and Bjorkman, A. D. and Blackman, C. and Blanco, C. and Blonder, B. and Blumenthal, D. and Bocanegra-González, K. T. and Boeckx, P. and Bohlman, S. and Böhning-Gaese, K. and Boisvert-Marsh, L. and Bond, W. and Bond-Lamberty, B. and Boom, A. and Boonman, C. C. F. and Bordin, K. and Boughton, E. H. and Boukili, V. and Bowman, D. M. J. S. and Bravo, S. and Brendel, M. R. and Broadley, M. R. and Brown, K. A. and Bruelheide, H. and Brumnich, F. and Bruun, H. H. and Bruy, D. and Buchanan, S. W. and Bucher, S. F. and Buchmann, N. and Buitenwerf, R. and Bunker, D. E. and Bürger, J. and Burrascano, S. and Burslem, D. F. R. P. and Butterfield, B. J. and Byun, C. and Marques, M. and Scalon, M. C. and Caccianiga, M. and Cadotte, M. and Cailleret, M. and Camac, J. and Camarero, J. J. and Campany, C. and Campetella, G. and Campos, J. A. and Cano-Arboleda, L. and Canullo, R. and Carbognani, M. and Carvalho, F. and Casanoves, F. and Castagneyrol, B. and Catford, J. A. and Cavender-Bares, J. and Cerabolini, B. E. L. and Cervellini, M. and Chacón-Madrigal, E. and Chapin, K. and Chapin, F. S. and Chelli, S. and Chen, S.-C. and Chen, A. and Cherubini, P. and Chianucci, F. and Choat, B. and Chung, K.-S. and Chytrý, M. and Ciccarelli, D. and Coll, L. and Collins, C. G. and Conti, L. and Coomes, D. and Cornelissen, J. H. C. and Cornwell, W. K. and Corona, P. and Coyea, M. and Craine, J. and Craven, D. and Cromsigt, J. P. G. M. and Csecserits, A. and Cufar, K. and Cuntz, M. and da Silva, A. C. and Dahlin, K. M. and Dainese, M. and Dalke, I. and Dalle Fratte, M. and Dang-Le, A. T. and Danihelka, J. and Dannoura, M. and Dawson, S. and de Beer, A. J. and De Frutos, A. and De Long, J. R. and Dechant, B. and Delagrange, S. and Delpierre, N. and Derroire, G. and Dias, A. S. and Diaz-Toribio, M. H. and Dimitrakopoulos, P. G. and Dobrowolski, M. and Doktor, D. and Dřevojan, P. and Dong, N. and Dransfield, J. and Dressler, S. and Duarte, L. and Ducouret, E. and Dullinger, S. and Durka, W. and Duursma, R. and Dymova, O. and E-Vojtkó, A. and Eckstein, R. L. and Ejtehadi, H. and Elser, J. and Emilio, T. and Engemann, K. and Erfanian, M. B. and Erfmeier, A. and Esquivel-Muelbert, A. and Esser, G. and Estiarte, M. and Domingues, T. F. and Fagan, W. F. and Fagúndez, J. and Falster, D. S. and Fan, Y. and Fang, J. and Farris, E. and Fazlioglu, F. and Feng, Y. and Fernandez-Mendez, F. and Ferrara, C. and Ferreira, J. and Fidelis, A. and Finegan, B. and Firn, J. and Flowers, T. J. and Flynn, D. F. B. and Fontana, V. and Forey, E. and Forgiarini, C. and François, L. and Frangipani, M. and Frank, D. and Frenette-Dussault, C. and Freschet, G. T. and Fry, E. L. and Fyllas, N. M. and Mazzochini, G. G. and Gachet, S. and Gallagher, R. and Ganade, G. and Ganga, F. and García-Palacios, P. and Gargaglione, V. and Garnier, E. and Garrido, J. L. and de Gasper, A. L. and Gea-Izquierdo, G. and Gibson, D. and Gillison, A. N. and Giroldo, A. and Glasenhardt, M.-C. and Gleason, S. and Gliesch, M. and Goldberg, E. and Göldel, B. and Gonzalez-Akre, E. and Gonzalez-Andujar, J. L. and González-Melo, A. and González-Robles, A. and Graae, B. J. and Granda, E. and Graves, S. and Green, W. A. and Gregor, T. and Gross, N. and Guerin, G. R. and Günther, A. and Gutiérrez, A. G. and Haddock, L. and Haines, A. and Hall, J. and Hambuckers, A. and Han, W. and Harrison, S. P. and Hattingh, W. and Hawes, J. E. and He, T. and He, P. and Heberling, J. M. and Helm, A. and Hempel, S. and Hentschel, J. and Hérault, B. and Hereş, A.-M. and Herz, K. and Heuertz, M. and Hickler, T. and Hietz, P. and Higuchi, P. and Hipp, A. L. and Hirons, A. and Hock, M. and Hogan, J. A. and Holl, K. and Honnay, O. and Hornstein, D. and Hou, E. and Hough-Snee, N. and Hovstad, K. A. and Ichie, T. and Igić, B. and Illa, E. and Isaac, M. and Ishihara, M. and Ivanov, L. and Ivanova, L. and Iversen, C. M. and Izquierdo, J. and Jackson, R. B. and Jackson, B. and Jactel, H. and Jagodzinski, A. M. and Jandt, U. and Jansen, S. and Jenkins, T. and Jentsch, A. and Jespersen, J. R. P. and Jiang, G.-F. and Johansen, J. L. and Johnson, D. and Jokela, E. J. and Joly, C. A. and Jordan, G. J. and Joseph, G. S. and Junaedi, D. and Junker, R. R. and Justes, E. and Kabzems, R. and Kane, J. and Kaplan, Z. and Kattenborn, T. and Kavelenova, L. and Kearsley, E. and Kempel, A. and Kenzo, T. and Kerkhoff, A. and Khalil, M. I. and Kinlock, N. L. and Kissling, W. D. and Kitajima, K. and Kitzberger, T. and Kjøller, R. and Klein, T. and Kleyer, M. and Klimešová, J. and Klipel, J. and Kloeppel, B. and Klotz, S. and Knops, J. M. H. and Kohyama, T. and Koike, F. and Kollmann, J. and Komac, B. and Komatsu, K. and König, C. and Kraft, N. J. B. and Kramer, K. and Kreft, H. and Kühn, I. and Kumarathunge, D. and Kuppler, J. and Kurokawa, H. and Kurosawa, Y. and Kuyah, S. and Laclau, J.-P. and Lafleur, B. and Lallai, E. and Lamb, E. and Lamprecht, A. and Larkin, D. J. and Laughlin, D. and Le Bagousse-Pinguet, Y. and le Maire, G. and le Roux, P. C. and le Roux, E. and Lee, T. and Lens, F. and Lewis, S. L. and Lhotsky, B. and Li, Y. and Li, X. and Lichstein, J. W. and Liebergesell, M. and Lim, J. Y. and Lin, Y.-S. and Linares, J. C. and Liu, C. and Liu, D. and Liu, U. and Livingstone, S. and Llusià, J. and Lohbeck, M. and López-García, Á. and Lopez-Gonzalez, G. and Lososová, Z. and Louault, F. and Lukács, B. A. and Lukeš, P. and Luo, Y. and Lussu, M. and Ma, S. and Maciel Rabelo Pereira, C. and Mack, M. and Maire, V. and Mäkelä, A. and Mäkinen, H. and Malhado, A. C. M. and Mallik, A. and Manning, P. and Manzoni, S. and Marchetti, Z. and Marchino, L. and Marcilio-Silva, V. and Marcon, E. and Marignani, M. and Markesteijn, L. and Martin, A. and Martínez-Garza, C. and

Martínez-Vilalta, J. and Mašková, T. and Mason, K. and Mason, N. and Massad, T. J. and Masse, J. and Mayrose, I. and McCarthy, J. and McCormack, M. L. and McCulloh, K. and McFadden, I. R. and McGill, B. J. and McPartland, M. Y. and Medeiros, J. S. and Medlyn, B. and Meerts, P. and Mehrabi, Z. and Meir, P. and Melo, F. P. L. and Mencuccini, M. and Meredieu, C. and Messier, J. and Mészáros, I. and Metsaranta, J. and Michaletz, S. T. and Michelaki, C. and Migalina, S. and Milla, R. and Miller, J. E. D. and Minden, V. and Ming, R. and Mokany, K. and Moles, A. T. and Molnár V, A. and Molofsky, J. and Molz, M. and Montgomery, R. A. and Monty, A. and Moravcová, L. and Moreno-Martínez, A. and Moretti, M. and Mori, A. S. and Mori, S. and Morris, D. and Morrison, J. and Mucina, L. and Mueller, S. and Muir, C. D. and Müller, S. C. and Munoz, F. and Myers-Smith, I. H. and Myster, R. W. and Nagano, M. and Naidu, S. and Narayanan, A. and Natesan, B. and Negoita, L. and Nelson, A. S. and Neuschulz, E. L. and Ni, J. and Niedrist, G. and Nieto, J. and Niinemets, Ü. and Nolan, R. and Nottebrock, H. and Nouvellon, Y. and Novakovskiy, A. and The Nutrient, N. and Nystuen, K. O. and O'Grady, A. and O'Hara, K. and O'Reilly-Nugent, A. and Oakley, S. and Oberhuber, W. and Ohtsuka, T. and Oliveira, R. and Öllerer, K. and Olson, M. E. and Onipchenko, V. and Onoda, Y. and Onstein, R. E. and Ordonez, J. C. and Osada, N. and Ostonen, I. and Ottaviani, G. and Otto, S. and Overbeck, G. E. and Ozinga, W. A. and Pahl, A. T. and Paine, C. E. T. and Pakeman, R. J. and Papageorgiou, A. C. and Parfionova, E. and Pärtel, M. and Patacca, M. and Paula, S. and Paule, J. and Pauli, H. and Pausas, J. G. and Peco, B. and Penuelas, J. and Perea, A. and Peri, P. L. and Petisco-Souza, A. C. and Petraglia, A. and Petritan, A. M. and Phillips, O. L. and Pierce, S. and Pillar, V. D. and Pisek, J. and Pomogaybin, A. and Poorter, H. and Portsmuth, A. and Poschlod, P. and Potvin, C. and Pounds, D. and Powell, A. S. and Power, S. A. and Prinzing, A. and Puglielli, G. and Pyšek, P. and Raevel, V. and Rammig, A. and Ransijn, J. and Ray, C. A. and Reich, P. B. and Reichstein, M. and Reid, D. E. B. and Réjou-Méchain, M. and de Dios, V. R. and Ribeiro, S. and Richardson, S. and Riibak, K. and Rillig, M. C. and Riviera, F. and Robert, E. M. R. and Roberts, S. and Robroek, B. and Roddy, A. and Rodrigues, A. V. and Rogers, A. and Rollinson, E. and Rolo, V. and Römermann, C. and Ronzhina, D. and Roscher, C. and Rosell, J. A. and Rosenfield, M. F. and Rossi, C. and Roy, D. B. and Royer-Tardif, S. and Rüger, N. and Ruiz-Peinado, R. and Rumpf, S. B. and Rusch, G. M. and Ryo, M. and Sack, L. and Saldaña, A. and Salgado-Negret, B. and Salguero-Gomez, R. and Santa-Regina, I. and Santacruz-García, A. C. and Santos, J. and Sardans, J. and Schamp, B. and Scherer-Lorenzen, M. and Schleuning, M. and Schmid, B. and Schmidt, M. and Schmitt, S. and Schneider, J. V. and Schowanek, S. D. and Schrader, J. and Schrodt, F. and Schuldt, B. and Schurr, F. and Selaya Garvizu, G. and Semchenko, M. and Seymour, C. and Sfair, J. C. and Sharpe, J. M. and Sheppard, C. S. and Sheremetiev, S. and Shiodera, S. and Shipley, B. and Shovon, T. A. and Siebenkäs, A. and Sierra, C. and Silva, V. and Silva, M. and Sitzia, T. and Sjöman, H. and Slot, M. and Smith, N. G. and Sodhi, D. and Soltis, P. and Soltis, D. and Somers, B. and Sonnier, G. and Sørensen, M. V. and Sosinski Jr, E. E. and Soudzilovskaia, N. A. and Souza, A. F. and Spasojevic, M. and Sperandii, M. G. and Stan, A. B. and Stegen, J. and Steinbauer, K. and Stephan, J. G. and Sterck, F. and Stojanovic, D. B. and Strydom, T. and Suarez, M. L. and Svenning, J.-C. and Svitková, I. and Svitok, M. and Svoboda, M. and Swaine, E. and Swenson, N. and Tabarelli, M. and Takagi, K. and Tappeiner, U. and Tarifa, R. and Tauugourdeau, S. and Tavsanoglu, C. and te Beest, M. and Tedersoo, L. and Thiffault, N. and Thom, D. and Thomas, E. and Thompson, K. and Thornton, P. E. and Thuiller, W. and Tichý, L. and Tissue, D. and Tjoelker, M. G. and Tng, D. Y. P. and Tobias, J. and Török, P. and Tarin, T. and Torres-Ruiz, J. M. and Tóthmérész, B. and Treurnicht, M. and Trivellone, V. and Trolliet, F. and Trotsiuk, V. and Tsakalos, J. L. and Tsiripidis, I. and Tysklind, N. and Umehara, T. and Usoltsev, V. and Vadeboncoeur, M. and Vaezi, J. and Valladares, F. and Vamosi, J. and van Bodegom, P. M. and van Breugel, M. and Van Cleemput, E. and van de Weg, M. and van der Merwe, S. and van der Plas, F. and van der Sande, M. T. and van Kleunen, M. and Van Meerbeek, K. and Vanderwel, M. and Vanselow, K. A. and Vårhammar, A. and Varone, L. and Vasquez Valderrama, M. Y. and Vassilev, K. and Vellend, M. and Veneklaas, E. J. and Verbeeck, H. and Verheyen, K. and Vibrans, A. and Vieira, I. and Villacís, J. and Violle, C. and Vivek, P. and Wagner, K. and Waldram, M. and Waldron, A. and Walker, A. P. and Waller, M. and Walther, G. and Wang, H. and Wang, F. and Wang, W. and Watkins, H. and Watkins, J. and Weber, U. and Weedon, J. T. and Wei, L. and Weigelt, P. and Weiher, E. and Wells, A. W. and Wellstein, C. and Wenk, E. and Westoby, M. and Westwood, A. and White, P. J. and Whitten, M. and Williams, M. and Winkler, D. E. and Winter, K. and Womack, C. and Wright, I. J. and Wright, S. J. and Wright, J. and Pinho, B. X. and Ximenes, F. and Yamada, T. and Yamaji, K. and Yanai, R. and Yankov, N. and Yguel, B. and Zanini, K. J. and Zanne, A. E. and Zelený, D. and Zhao, Y.-P. and Zheng, J. and Zheng, J. and Ziemińska, K. and Zirbel, C. R. and Zizka, G. and Zo-Bi, I. C. and Zotz, G. and Wirth, C.: TRY plant trait database – enhanced coverage and open access, Global Change Biology, 26, 119-188, 10.1111/gcb.14904, 2020.

Lázaro-Gredilla, M., Titsias, M. K., Verrelst, J., and Camps-Valls, G.: Retrieval of Biophysical Parameters With Heteroscedastic Gaussian Processes, IEEE Geoscience and Remote Sensing Letters, 11, 838-842, 10.1109/LGRS.2013.2279695, 2014.

Li, W., Pacheco-Labrador, J., Migliavacca, M., Miralles, D., Hoek van Dijke, A., Reichstein, M., Forkel, M., Zhang, W., Frankenberg, C., Panwar, A., Zhang, Q., Weber, U., Gentine, P., and Orth, R.: Widespread and complex drought effects on vegetation physiology inferred from space, Nature Communications, 14, 4640, 10.1038/s41467-023-40226-9, 2023.

Luo, X., Croft, H., Chen, J. M., He, L., and Keenan, T. F.: Improved estimates of global terrestrial photosynthesis using information on leaf chlorophyll content, Global Change Biology, 25, 2499-2514, 10.1111/gcb.14624, 2019.

Meerdink, S. K., Hook, S. J., Roberts, D. A., and Abbott, E. A.: The ECOSTRESS spectral library version 1.0, Remote Sensing of Environment, 230, 111196, https://doi.org/10.1016/j.rse.2019.05.015, 2019.

Migliavacca, M., Reichstein, M., Richardson, A. D., Colombo, R., Sutton, M. A., Lasslop, G., Tomelleri, E., Wohlfahrt, G., Carvalhais, N., Cescatti, A., Mahecha, M. D., Montagnani, L., Papale, D., Zaehle, S., Arain, A., Arneth, A., Black, T. A., Carrara, A., Dore, S., Gianelle, D., Helfter, C., Hollinger, D., Kutsch, W. L., Lafleur, P. M., Nouvellon, Y., Rebmann, C., Da Rocha, H. R., Rodeghiero, M., Roupsard, O., SebastiÀ, M.-T., Seufert, G., Soussana, J.-F., and Van Der Molen, M. K.: Semiempirical modeling of abiotic and biotic factors controlling ecosystem respiration across eddy covariance sites, Global Change Biology, 17, 390-409, https://doi.org/10.1111/j.1365-2486.2010.02243.x, 2011.

Miner, G., L., Bauerle, W., L., and Baldocchi, D., D.: Estimating the sensitivity of stomatal conductance to photosynthesis: a review, Plant, Cell & Environment, 40, 1214-1238, 10.1111/pce.12871, 2016.

Niu, S., Zhang, Y., Yuan, Z., Liu, W., Huang, J., and Wan, S.: Effects of interspecific competition and nitrogen seasonality on the photosynthetic characteristics of C3 and C4 grasses, Environmental and Experimental Botany, 57, 270-277, https://doi.org/10.1016/j.envexpbot.2005.06.004, 2006.

Pacheco-Labrador, J., de Bello, F., Migliavacca, M., Ma, X., Carvalhais, N., and Wirth, C.: A generalizable normalization for assessing plant functional diversity metrics across scales from remote sensing, Methods in Ecology and Evolution, 14, 2123-2136, https://doi.org/10.1111/2041-210X.14163, 2023.

Pacheco-Labrador, J., El-Madany, T. S., van der Tol, C., Martin, M. P., Gonzalez-Cascon, R., Perez-Priego, O., Guan, J., Moreno, G., Carrara, A., Reichstein, M., and Migliavacca, M.: senSCOPE: Modeling mixed canopies combining green and brown senesced leaves. Evaluation in a Mediterranean Grassland, Remote Sensing of Environment, 257, 112352, https://doi.org/10.1016/j.rse.2021.112352, 2021.

Pacheco-Labrador, J., Migliavacca, M., Ma, X., Mahecha, M. D., Carvalhais, N., Weber, U., Benavides, R., Bouriaud, O., Barnoaiea, I., Coomes, D. A., Bohn, F. J., Kraemer, G., Heiden, U., Huth, A., and Wirth, C.: Challenging the link between functional and spectral diversity with radiative transfer modeling and data, Remote Sensing of Environment, 280, 113170, https://doi.org/10.1016/j.rse.2022.113170, 2022.

Pacheco-Labrador, J., Perez-Priego, O., El-Madany, T. S., Julitta, T., Rossini, M., Guan, J., Moreno, G., Carvalhais, N., Martín, M. P., Gonzalez-Cascon, R., Kolle, O., Reischtein, M., van der Tol, C., Carrara, A., Martini, D., Hammer, T. W., Moossen, H., and Migliavacca, M.: Multiple-constraint inversion of SCOPE. Evaluating the potential of GPP and SIF for the retrieval of plant functional traits, Remote Sensing of Environment, 234, 111362, https://doi.org/10.1016/j.rse.2019.111362, 2019.

Proctor, C., Lu, B., and He, Y.: Determining the absorption coefficients of decay pigments in decomposing monocots, Remote Sensing of Environment, 199, 137-153, https://doi.org/10.1016/j.rse.2017.07.007, 2017.

Rubel, F., Brugger, K., Haslinger, K., and Auer, I.: The climate of the European Alps: Shift of very high resolution Köppen-Geiger climate zones 1800–2100, Meteorologische Zeitschrift, 26, 115-125, 10.1127/metz/2016/0816, 2017.

Solovchenko, A., Gitelson, A., Chivkunova, O., and Merzlyak, M.: Foliar reflectance and biochemistry, 5 data sets [dataset], 10.13140/RG.2.2.13225.29282, 2017.

van der Tol, C., Verhoef, W., Timmermans, J., Verhoef, A., and Su, Z.: An integrated model of soil-canopy spectral radiances, photosynthesis, fluorescence, temperature and energy balance, Biogeosciences, 6, 3109-3129, 10.5194/bg-6-3109-2009, 2009.

Wang, Q., Tang, Y., and Atkinson, P. M.: The effect of the point spread function on downscaling continua, ISPRS Journal of Photogrammetry and Remote Sensing, 168, 251-267, https://doi.org/10.1016/j.isprsjprs.2020.08.016, 2020.